

# Converting a Commercial Separator into a Thin-film Multi-Layer Hybrid Solid Electrolyte for Li Metal Batteries

Lukas Herbers,<sup>[a]</sup> William Fettkether,<sup>[b]</sup> Silvan Stuckenberg,<sup>[a]</sup> Debbie Berghus,<sup>[a]</sup> Steve W. Martin,<sup>[a, b]</sup> Martin Winter,<sup>[a, c]</sup> and Peter Bieker<sup>\*[c]</sup>

To address the manifold challenges solid electrolytes (SE) do face in NMC||Lithium metal batteries, we demonstrate that these can be overcome by converting a commercial Celgard 2500 separator into a jack of all trades hybrid solid electrolyte (HSE). This approach follows a multi-layer electrolyte strategy, to better cope with the very different chemistries of the cathode, the bulk electrolyte material, and the Li metal anode. A cathode-facing electrolyte layer based on lithium aluminum titanium phosphate (LATP) provides a high voltage stability of

$\geq 4.5$  V. High mechanical strength of the overall thin film electrolyte ( $\leq 50 \mu\text{m}$ ) is achieved with a middle layer based on Celgard 2500. The layer on the anode side, based on polyethylene oxide (PEO), allows stable cycling of the lithium metal. High Coulombic efficiencies in NMC622||Li metal cells (99.9%) and LFP||Li metal cells (99.9%) enable long term cycling with high-capacity retention of 46% and 52% after 1,000 cycles, respectively.

## Introduction

Li metal is a promising anode (negative electrode) material for high energy density batteries because it has a high specific capacity of  $3,860 \text{ mAh g}^{-1}$  and the lowest standard reduction potential of all metals of  $-3.04 \text{ V}$  vs. standard hydrogen electrode (SHE).<sup>[1]</sup> Therefore, compared to graphite anodes ( $372 \text{ mAh g}^{-1}$ ) in lithium ion batteries, higher energy densities can be achieved.<sup>[2]</sup> If the Li metal anode is then combined with a high voltage cathode material such as lithium nickel manganese cobalt oxide (NMC), the energy density of this next generation battery could be increased even further.<sup>[3,4]</sup> However, there are many challenges that electrolytes must face in such a system, due to the diametrical electrochemical reactivities of the Li metal anode and the cathode materials, as well as numerous other general challenges such as safety concerns.<sup>[5–7]</sup> From a safety standpoint, solid electrolytes (SEs) have attracted attention as a potential replacement for liquid electrolytes (LEs).<sup>[8]</sup> They are often considered safer than organic LEs because of their lower volatility and flammability, which reduces the risk of ignition.<sup>[9]</sup> However, being solid state can present different additional challenges depending on the SE

system used. For example, solid polymer electrolytes (SPEs), which transport ions by segmental motions, ion hopping, or a vehicle mechanism, may suffer from reduced ion mobility in the electrolyte. Inorganic solid electrolytes (SIEs), which transport  $\text{Li}^+$  through a crystalline or glassy-structure, may suffer from poor surface contact properties.<sup>[10]</sup> To overcome the challenges of a single electrolyte type, hybridization has been investigated, where hybrid solid electrolytes (HSEs) consisting of more than two components, e.g. SPEs, SIEs, and/or ionic liquids (ILs), are used, see SI Figure 1.<sup>[6,11,12]</sup> The combination of two of them is often referred to as ternary solid polymer electrolyte (SPE, Li salt and IL $\rightarrow$ TSPE), quasi/pseudo solid electrolyte (SIE and IL $\rightarrow$ QSE) and composite polymer-inorganic electrolyte (SIE/ceramic filler and SPE $\rightarrow$ CPIE).<sup>[6,11,12]</sup> By compensating for the disadvantageous effects of the other electrolyte type, a synergistic property profile is achieved for these combinations.<sup>[13]</sup> This can be illustrated using CPIEs as an example. On the one hand, SIEs often times exhibit high bulk ionic conductivity by channeling weakly bound  $\text{Li}^+$  through conduction pathways, but they usually suffer from poor electrode contacting properties due to their stiffness and their rough surface.<sup>[14]</sup> On the other hand, SPEs, such as polyethylene oxides (PEO), are generally considered soft materials and therefore suitable for providing electrode contact, but can suffer from low ionic conductivity due to limited transport through immobile polymer chains. Therefore, as shown in the work of Zhou *et al.* or Duan *et al.*, SIEs and SPEs have been combined into CPIEs to have the good bulk properties of the SIE with the advantageous interfacial properties of the SPE.<sup>[15,16]</sup> However, while this approach can considerably improve the diversity of electrolyte capabilities, some challenges remain when using SPEs and/or SIEs, alone. For example, in crystalline SIEs particle-to-particle ion transport occurs at grains, limiting the full theoretical potential of the otherwise highly  $\text{Li}^+$ -conducting bulk SIEs.<sup>[17]</sup> In SPEs, the ionic conductivity may be limited by self-ordering of polymer chains through crystalline domains unavailable for  $\text{Li}^+$  transport.<sup>[18]</sup>

[a] L. Herbers, S. Stuckenberg, D. Berghus, S. W. Martin, M. Winter  
MEET Battery Research Center, Institute of Physical Chemistry, University of Münster, 48149 Münster, Germany

[b] W. Fettkether, S. W. Martin  
Department of Materials Science and Engineering, Iowa State University, Ames, IA 50010, United States

[c] M. Winter, P. Bieker  
Helmholtz-Institute Münster (HIMS), IEK-12, Forschungszentrum Jülich GmbH, 48149 Münster, Germany  
E-mail: peter.bieker@uni-muenster.de

© 2024 Universität Münster and The Authors. *Batteries & Supercaps* published by Wiley-VCH GmbH. This is an open access article under the terms of the Creative Commons Attribution License, which permits use, distribution and reproduction in any medium, provided the original work is properly cited.

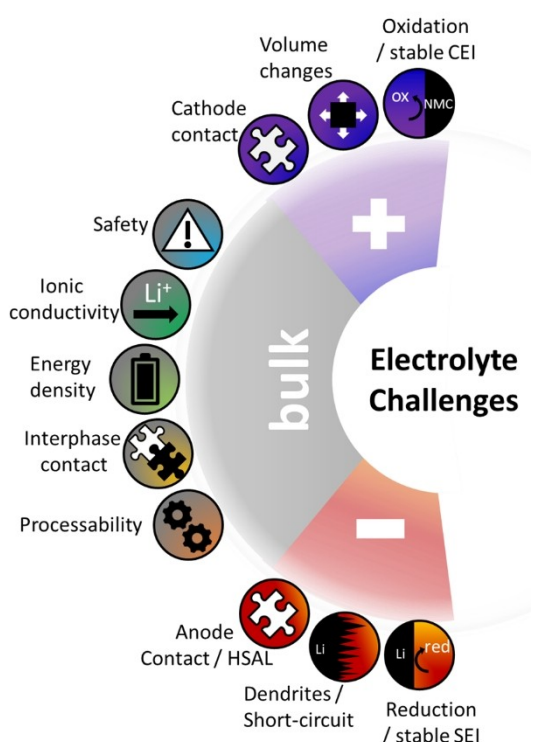


**Figure 1.** Challenges electrolytes face in NMC622||Li metal cells. Top: cathode related challenges (oxidation, volume changes, cathode contact); center: general bulk challenges (safety, ionic conductivity, energy density, interphase contact, processability); bottom: anode related challenges (anode contact/HSAL, dendrites/short-circuit, reduction).

Therefore, LEs would be a possible third component to overcome grain boundaries in crystalline SIEs and to plasticize SPEs. However, as mentioned above, the high thermal stability of the SEs would be negated by the addition of low-boiling point organic solvents. Therefore, ILs, often referred to as liquid salts, which have a low melting point due to their low lattice energies, negligible vapor pressure, and high thermal stability, are more commonly used.<sup>[19]</sup> Although more costly than LEs, but probably cheaper than most solid electrolytes, they have the potential to maintain the safety of the electrolyte system.<sup>[19]</sup>

While hybridization of SEs can help meet several multiple bulk electrolyte requirements, there are additional contrasting challenges from the cathode and anode. The wide range of challenges associated with electrodes can be explained by their different chemical and physical properties. While Li metal is a soft material, with high reducing power and is likely to be electro-dissolved and redeposited via high surface area lithium (HSAL). NMC cathode materials are brittle, chemically oxidative and lead to volume changes during charging and discharging by  $\text{Li}^+$  intercalation and deintercalation.<sup>[7]</sup> Two main strategies are used to address these contrasting challenges. First, as discussed above, the LE or SE is modified in composition or by hybridization to improve specific properties such as reversible Li metal electro-deposition/-dissolution or electrochemical stability window (ESW) enhancement.<sup>[20–24]</sup> However, these bulk electrolyte modifications are mainly for a specific purpose and

often lack synergistic multifunctional applications. Second, the anode and cathode themselves are modified by applying coatings on the Li metal to improve electro-deposition/-dissolution to form an artificial solid electrolyte interphase (SEI), or by applying thin coatings on the cathode material to protect the electrolyte or cathode material from degradation by forming an artificial cathode electrolyte interphase (CEI).<sup>[25–35]</sup> These approaches require an additional coating process by means of atomic layer deposition (ALD), sputtering, casting, or chemical deposition of the electrodes. Therefore, an alternative third SE multi-layer approach has attracted attention recently.<sup>[36]</sup> Here, two or more differently designed SE layers are stacked on top of each other to better meet the different requirements of anode and cathode.<sup>[16,37,38]</sup> Due to being solid state, these layers do not mix with each other, allowing different electrolyte types to be used as building blocks for specifically designed functional layers. In this way, a variety of approaches are possible. For example, a reductively more stable anode-facing SE can be used towards Li metal and a more oxidatively stable cathode-facing SE can be used towards NMC.<sup>[39]</sup> Or a mechanically strong anode-facing SE can prevent short-circuiting by dendrites from Li metal, while a soft cathode-facing layer can provide sufficient cathode contact.<sup>[40]</sup>

In this work, the hybridization approach and the multi-layer approach are combined. This research builds on previous publications by Zhang *et al.* and Herbers *et al.*<sup>[41,42]</sup> As shown by Zhang *et al.*, commercially available Celgard 2500 separators (Cg) can be coated on both sides with a PEO-based TSPE solution to easily manufacture a sandwich-like multi-layer TSPE.<sup>[41]</sup> The Cg-reinforced electrolyte displays high mechanical strength compared to pure TSPE, which prevents short-circuits, e.g. by dendrites, and enables a much easier processing of the TSPEs. Nevertheless, as shown by Herbers *et al.*, such PEO-based TSPEs are not suitable towards NMC cathodes because PEO is oxidized at  $\geq 3.8$  V, which leads to rapid capacity fading in NMC622||Li cells.<sup>[42]</sup> Therefore, it is necessary to replace PEO for the cathode-facing side of the electrolyte and use oxidative stable SEs. In this work, this research is further advanced by designing a multi-layer HSE with multiple phases:

1. A cathode-facing layer made of the SIE lithium aluminum titanium phosphate (LATP,  $\text{Li}_{1.3}\text{Al}_{0.3}\text{Ti}_{1.7}(\text{PO}_4)_3$ ) and a TSPE based on the SPE poly(vinylidene fluoride-co-hexafluoropropylene) (PVDF-HFP) for cathode contact and oxidative stability;
2. A mechanically strong Cg layer filled with TSPE for short-circuit prevention, processability and high energy density;
3. An anode-facing TSPE based on PEO for Li metal contact and reductive stability;
4. All layers are interconnected with the IL 1-butyl-1-methyl-pyrrolidinium-bis-(trifluoromethylsulfonyl)imid (Pyr<sub>14</sub>TFSI) and the Li salt lithium bis(trifluoromethanesulfonyl)imide (LiTFSI) for interphase contact, high ionic conductivity, and to maintain safety, see Figure 2.

Each layer and its advantages will be discussed. First, the effects of implementing high voltage stable SIE and SPE materials for the cathode layer are outlined. Then, the ratio of the cathode electrolyte materials will be optimized in terms of

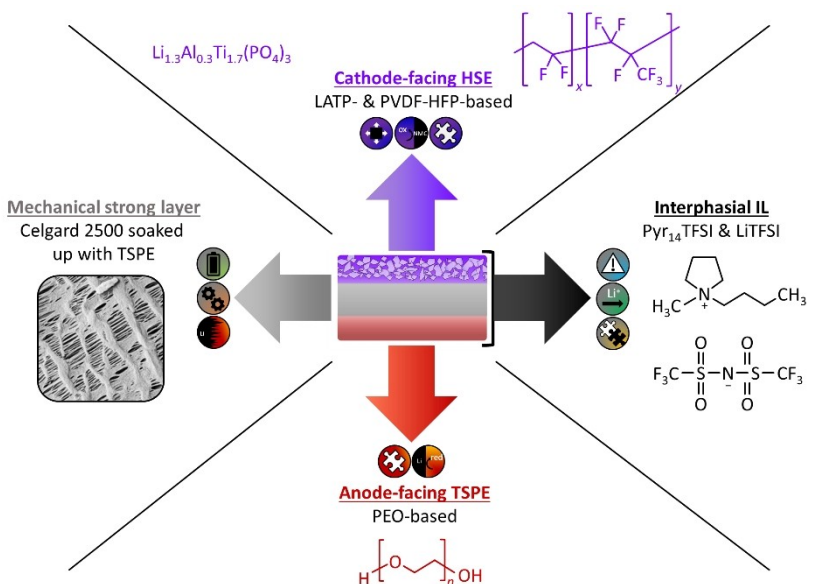


**Figure 2.** Phases within the CgLATP<sub>50</sub> + electrolyte designed in this work. Center: layered structure of the electrolyte; top: cathode-facing layer consisting of LATP and PVDF-HFP-TSPE; left-center: mechanically rigid layer of Cg soaked with TSPE; bottom: anode-facing layer consisting of PEO-TSPE; right-center: interphasial ionic liquid consisting of Pyr<sub>14</sub>TFSI and LiTFSI.

cathode contact and bulk ionic conductivity. Second, the influence of the ionic liquid on phase behavior is analyzed. Third, the advantages of the mechanically strong Cg layer for short-circuit prevention and processability are described. Fourth, cycling stability of the Li metal towards the anode-facing electrolyte layer is outlined. Finally, the long-term cycling performance in NMC622||Li metal cells and lithium iron phosphate (LFP)||Li metal cells is compared to materials from the literature.

## Experimental

### Chemicals

PEO (Dow Chemical, molecular weight 4,000,000) was dried at 60°C under reduced pressure  $\leq 10^{-3}$  mbar for at least 48 h, followed by 48 h at 60°C under reduced pressure  $\leq 10^{-7}$  mbar. Benzophenone (BP, Merck, 99%), acetonitrile (ACN, Carl Roth, ≥ 99.9%, ROTIDRY®, ≤ 10 ppm H<sub>2</sub>O) and 1-methyl-2-pyrrolidinone (NMP, Thermo Fisher Scientific, 99.5%, AcroSeal™, over molecular sieve) were used as

received. Pyr<sub>14</sub>TFSI (Solvionic, 99.9%), LiTFSI (TCI, > 98%), LATP (MSE PRO Solid Electrolyte, 300 nm) and PVDF-HFP (Sigma-Aldrich, molecular weight 400,000) were dried for at least 48 h at 110°C under reduced pressure  $\leq 10^{-3}$  mbar followed by 48 hours at 110°C under reduced pressure  $\leq 10^{-7}$  mbar. NMC622 sheets (experimental capacity 180 mAh g<sup>-1</sup>, active mass loading: 4 mg cm<sup>-2</sup>), and LFP sheets (LiFePO<sub>4</sub>, NANOMYTE® BE-60E, experimental capacity  $\geq 170$  mAh g<sup>-1</sup>, NEI Corporation, active mass loading: 4 mg cm<sup>-2</sup>) were dried at 100°C under reduced pressure  $\leq 10^{-3}$  mbar for 48 hours. Li metal was used as received with a thickness of 50 µm.

### Electrolyte manufacturing

Two electrolyte pastes were prepared for coating the two Cg sides, see Table 1 and Figure 3. For the anode paste, PEO is first dissolved in ACN (222 mg per 10 mL) by stirring the mixture at 60°C. Then Pyr<sub>14</sub>TFSI, LiTFSI and BP (5 wt% of PEO content) are added and stirred until a homogeneous paste is obtained. The paste is applied to one side of the Cg using a doctor blade. The slit size of the doctor blade is adjusted to match the volume fraction of TSPE in the paste to fill the porous Cg and maintain an approximately 12.5 µm thick PEO-TSPE layer on the surface after drying. After 30 min of drying in a dry room at room temperature (RT) the film is

**Table 1.** Composition of the Cg-coated electrolyte films described in this work.

Name	Anode Side		Cathode Side		LATP added
	Type	TSPE Composition (EO:LiTFSI:Pyr <sub>14</sub> TFSI)	Type	TSPE Composition (EO <sub>eq</sub> :LiTFSI:Pyr <sub>14</sub> TFSI)	
CgPEO	PEO-TSPE	10:1:2	PEO-TSPE	10:1:2	-
CgPVDF	PEO-TSPE	10:1:2	PVDF-HFP-TSPE	10:1:2	-
CgLATP <sub>50</sub>	PEO-TSPE	10:1:2	PVDF-HFP-LATP-SE	10:1:2	+ 50 wt%
CgLATP <sub>100</sub>	PEO-TSPE	10:1:2	PVDF-HFP-LATP-SE	10:1:2	+ 100 wt%
CgLATP <sub>200</sub>	PEO-TSPE	10:1:2	PVDF-HFP-LATP-SE	10:1:2	+ 200 wt%
CgLATP <sub>50</sub> +	PEO-TSPE	10:1:4	PVDF-HFP-LATP-SE	10:1:4	+ 50 wt%

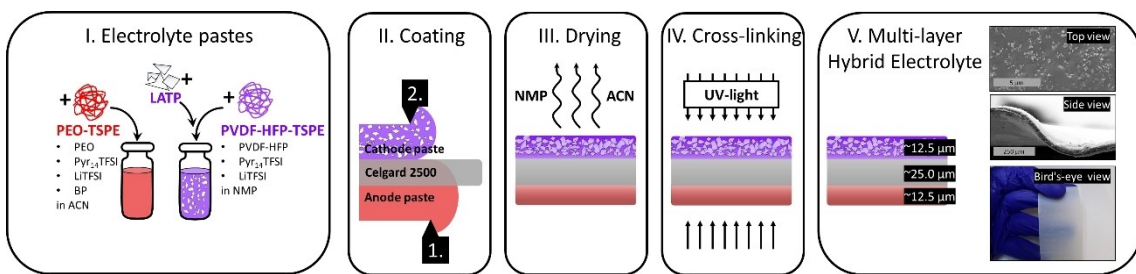


**Figure 3.** Processing of the multi-layer hybrid electrolyte. I. Composition of the electrolyte pastes used to prepare the electrolyte of this work; II. Coating of the Cg from both sides. III. Drying of the electrolyte; IV. Cross-linking of the electrolyte; V. Left: layer structure of the electrolyte, right from top to bottom: top view (SEM image) of the cathode-facing layer, side view of a cross-section of the electrolyte (SEM image) cut with a razor blade, bird's-eye view of a CgLATP<sub>50</sub> + electrolyte film (photographic image).

turned over. For the PVDF-HFP-based cathode paste, PVDF-HFP is dissolved in NMP (1,666 mg per 10 mL) by stirring the mixture at 60 °C. Then Pyr<sub>14</sub>TFSI and LiTFSI are added and stirred until a homogeneous paste is obtained. Then an additional mass of LATP is added in relative to the mass of TSPE and mixed. For highly LATP-loaded pastes (+ 100 wt%, + 200 wt%), additional NMP is added to make the paste applicable. The paste is applied to the other side of the Cg using a doctor blade. The slit size of the doctor blade is again adjusted to the volume fraction of the TSPE and SIE in the paste to obtain an approximately 12.5 μm thick layer on the surface after drying. To remove ACN and NMP the film is dried at 60 °C under reduced pressure for 48 h. Finally, the electrolyte films are cross-linked by UV curing (UVACUBE 100, 100 W lamp, Dr. Höne AG) for 10 min. For the samples in Figure 4a, LATP is added to the CgPEO cathode paste. For the samples in Figure 4b, PEO is replaced by PVDF-HFP in the NMP-based cathode paste of CgPEO. All other films were prepared with the composition shown in Table 1.

**Electrochemical measurements.** All CR2032 two-electrode coin cells were assembled in a dry room using 12 mm diameter round electrodes and 15 mm diameter electrolyte films. Linear sweep voltammetry (LSV) measurements (0.5 mVs<sup>-1</sup>, from open circuit voltage (OCV) to 5.7 V) with stainless steel (SST)||Li metal cells, staircase cyclic voltammetry (CV) measurements (0.5 mVs<sup>-1</sup>, from 3 V to upper cut-off voltages from 4.1 V to 5.5 V in 0.1 V steps) with (SST)||Li metal cells, staircase voltammetry measurements coupled with impedance spectroscopy (0.05 mA cm<sup>-2</sup>, 3.00 V to 4.25 V, 10 mHz to 1 MHz) with NMC622||Li metal cells, galvanostatic single discharge measurement (‘short-circuit measurement’, 0.1 mA cm<sup>-2</sup> to 0.4 mA cm<sup>-2</sup>) with Li metal||Li metal cells, staircase galvanostatic polarization measurement (from 0.05 mA cm<sup>-2</sup>, 0.5 mA cm<sup>-2</sup>, increasing by 0.05 mA cm<sup>-2</sup> every 3 cycles) with Li metal||Li metal cells, galvanostatic polarization measurement (0.1 mA cm<sup>-2</sup>, 0.5 mA cm<sup>-2</sup>, 1,000 h, two electrolyte films in ABBA arrangement) with Li metal||Li metal cells, galvanostatic single charge electro-deposition (0.05 mA cm<sup>-2</sup>, 2.0 mA cm<sup>-2</sup>) with Cu||Li metal cells, galvanostatic polarization measurement (0.2 mA cm<sup>-2</sup>, 1,000 cycles, 2.5 V to 4.0 V) with LFP||Li metal cells, and galvanostatic polarization measurement (0.3 mA cm<sup>-2</sup>, 1,000 cycles, 3.0 V to 4.25 V) with NMC622||Li metal cells were performed on a MACCOR battery cycler (MACCOR Series 4000) and a VMP potentiostat (Bio-152 Logic). Temperature-dependent ionic conductivity profiles were measured by impedance spectroscopy in Li metal||Li metal cells using a Novocontrol Alpha Analyzer (amplitude: 10 mV, frequency range: 0.1 Hz to 10 MHz, temperature range: 0 °C to 60 °C in 10 °C steps).

**Spectroscopy measurements.** Raman measurements of the solid samples were performed on a Horiba Scientific confocal Raman microscope (LabRam HR evolution, air-cooled CCD detector) equipped with a 50x long working distance objective (Carl Zeiss

Microscopy, 9.2 mm, numerical aperture 0.5) and a 532 nm laser beam set at 1.9 mW through a 10% filter with a 600 line/mm grating. Raman spectra were collected over four iterations of 25 s each. Handling the Raman microscope, collecting the spectra, and evaluating the data were done using LabSpec6.6.2 (Horiba Scientific). Raman spectra of the liquid samples were obtained using 5 mm NMR-tubes (Bruker) on a VERTEX 70 FT-IR spectrometer (Bruker) with a RAM II FT-Raman Module (Bruker), a N<sub>2</sub>-cooled Ge-diode detector and a 1064 nm laser beam with the OPUS 7.0 software. Fourier-transform infrared spectroscopy (FT-IR) measurements were performed on a BRUKER ALPHA II with an attenuated total reflection (ATR) crystal.

**Morphological measurements.** Scanning electron microscopy (SEM) images were obtained by a Zeiss Crossbeam 550 electron microscope (Carl Zeiss Microscopy GmbH). Images were acquired at 3 kV accelerating voltage and with an aperture size of 30 μm using an in-lens detector with a working distance of ≈ 5 mm. The acquisition time was optimized so that the electron beam did not induce any surface changes during exposure at high magnifications (> 2500x). 3-D laser scanning microscope (LSM) images and topographies were obtained by a VK-X260 Keyence using a 10x, 20x and 50x magnification lens by Nikon and a 408 nm laser source. A layer thickness gauge (Mitutoyo ABSOLUTE) was used to evaluate the electrolyte thickness.

**Contact angle measurements.** Contact angle measurements were performed on a DSA 100 by Krüss. A Pyr<sub>14</sub>TFSI drop was placed on 50 μm-thick polymer films. The polymer films were prepared by dissolving PEO in ACN and PVDF-HFP and/or LATP in NMP, casting the pastes onto a polymethyl methacrylate (PMMA) plate, and drying the films at 60 °C under reduced pressure.

**Thermal measurements.** Thermogravimetric analysis (TGA) was performed under inert gas using a Q5000IR (TA Instruments) at a heating rate of 10 K min<sup>-1</sup>. Differential scanning calorimetry (DSC) analysis was performed using a DSC Q2000 (TA Instruments) at a heating rate of 10 K min<sup>-1</sup>. Electrolytes were placed in hermetic aluminum pans with a helium gas flow of 25 mL min<sup>-1</sup>.

## Results and Discussion

### Impact of the cathode-facing electrolyte on NMC compatibility

To evaluate whether an electrolyte is suitable as a cathode or anode material, it must either be electrochemically stable to the electrode or it must form an SEI/CEI that diminishes further

electrolyte and electrode degradation. The ESW is used to mark the voltage window in which the electrolyte is stable. The  $\text{ESW}_{\text{lower}}$  is the lower voltage stability and the  $\text{ESW}_{\text{upper}}$  is the upper voltage stability. Since the cathode-side electrolyte is not in contact with the anode, only the  $\text{ESW}_{\text{upper}}$  is relevant for finding suitable electrolyte materials for the cathode side. As presented in previous work, it is desirable in an electrolyte system that all cathode-facing electrolyte materials have an  $\text{ESW}_{\text{upper}} \geq 4.25 \text{ V}$  in NMC622||Li metal cells, otherwise multiple consequences such as loss of active material, formation of volatile degradation products, increase in cell resistance, electrolyte degradation, and electrode corrosion will diminish the longevity of the battery system.<sup>[42]</sup> PEO, the most researched SPE, is an example of an electrolyte material that is not suitable for NMC622 as it oxidized at  $\geq 3.8 \text{ V}$  and emits volatile degradation products at  $\geq 4.0 \text{ V}$ .<sup>[42]</sup> A PEO-TSPE is used as a starting point in this work to show the improvement in oxidative stability when replacing it with oxidatively stable materials like LATP or PVDF-HFP. Since all the other materials in the PEO-TSPE like LiTFSI ( $\text{ESW}_{\text{upper}} \approx 4.83 \text{ V}$ ) and Pyr<sub>14</sub>TFSI ( $\text{ESW}_{\text{upper}} \approx 5.4 \text{ V}$ ) have a suitable oxidative stability, the incremental replacement shows the effects of LATP and PVDF-HFP have on the oxidative stability.<sup>[42,43]</sup>

LSV in SST||Li metal cells are used to evaluate the  $\text{ESW}_{\text{upper}}$  by comparing the current recorded as a result of degradation at elevated voltages. When no LATP, +50%, +100% and +200% LATP are added to the CgPEO electrolyte, the current observed at 4.5 V decreases from  $7.0 \mu\text{A cm}^{-2}$  to  $2.8 \mu\text{A cm}^{-2}$ ,  $0.7 \mu\text{A cm}^{-2}$ , and  $0.7 \mu\text{A cm}^{-2}$ , respectively, see Figure 4a. The improvement in oxidative stability with LATP addition is explained by one or more of the following phenomena. First, the electrochemical stability of LATP is higher than that of PEO, which reduces the oxidative degradation at the SST interface by increasing the fraction of oxidatively stable material. According to DFT calculations, the theoretical  $\text{ESW}_{\text{upper}}$  of LATP is at  $4.31 \text{ V}$ .<sup>[44]</sup> In practice,  $\text{ESW}_{\text{upper}}$  values up to 6 V are considered because the decomposition reaction is slow and thus LATP is kinetically

stabilized.<sup>[36]</sup> Second, dipole-dipole interactions between LATP and PEO can increase the electron transition energy level for PEO oxidation and thereby increase the total  $\text{ESW}_{\text{upper}}$ .<sup>[36]</sup> Third, as the surface roughness increases with the addition of LATP, the contact area between the SST and the electrolyte decreases, resulting in a reduced surface area exposed to degradation. When PEO is replaced by PVDF-HFP with contents of the latter of 0%, 25%, 50%, and 100% in the CgPEO electrolyte the current observed at 4.5 V decreases from  $7.0 \mu\text{A cm}^{-2}$  to  $4.6 \mu\text{A cm}^{-2}$ ,  $3.7 \mu\text{A cm}^{-2}$ , and  $1.1 \mu\text{A cm}^{-2}$ , respectively, see Figure 4b. The exchange of PEO by PVDF-HFP ( $\text{ESW}_{\text{upper}} \approx 4.88 \text{ V}$ ) increases the oxidative stability because the latter is more stable.<sup>[7]</sup>

To qualify the overall stability of an electrolyte containing both PVDF-HFP-TSPE and LATP, CgLATP<sub>50</sub> is further analyzed by staircase CV with a 0.1 V increase per cycle from 4.1 V to 5.5 V, see Figure 4c. The staircase approach allows a better distinction between the different stages of degradation. No current  $\geq 1.0 \mu\text{A cm}^{-2}$  is observed at  $< 4.6 \text{ V}$ . From there, the current gradually increases to  $5.0 \text{ V}$  ( $11.7 \mu\text{A cm}^{-2}$ ), most likely a result of PVDF-HFP and/or TFSI<sup>-</sup> degradation. At  $\geq 5.4 \text{ V}$ , a sharp increase in current is observed, presumably due to decomposition of Pyr<sub>14</sub>TFSI.<sup>[45–47]</sup> In summary, the LSV and staircase CV results suggest an overall electrolyte stability of  $\geq 4.5 \text{ V}$ , which makes the electrolyte suitable for LFP and NMC622 cathode materials.

While PVDF-HFP and LATP are both suitable for increasing the oxidative stability of the cathode-facing electrolyte, they have contrasting properties to face further electrolyte challenges such as cathode contact or bulk ionic conductivity. Therefore, the ratio of PVDF-HFP-TSPE to LATP is varied to find the best compromise for practical application. First, the surface morphology of the cathode side of the electrolytes is analyzed by LSM to evaluate the surface roughness and thus the ability to contact the cathode interface. Four HSEs (CgPVDF, CgLATP<sub>50</sub>, CgLATP<sub>100</sub>, CgLATP<sub>200</sub>) are compared, see Figure 5. For CgPVDF a homogeneous and flat surface is observed, see Figure 5a. For

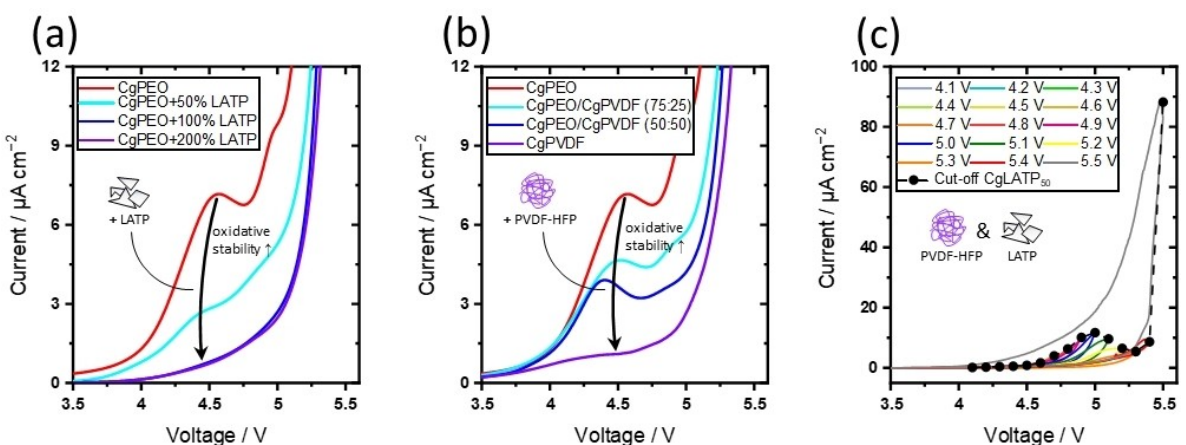


**Figure 4.** Influence of the composition of the cathode side of the multi-layer HSE on the  $\text{ESW}_{\text{upper}}$ . (a) Impact of LATP addition to CgPEO measured by LSV measurements ( $0.5 \text{ mVs}^{-1}$ , OCV to  $5.7 \text{ V}$ , at  $60^\circ\text{C}$ ) in SST||Li metal cells; (b) Impact of PVDF-HFP substitution measured by LSV measurements ( $0.5 \text{ mVs}^{-1}$ , OCV to  $5.7 \text{ V}$ , at  $60^\circ\text{C}$ ) in SST||Li metal cells; (c) stability CgLATP<sub>50</sub> measured by staircase CV ( $0.5 \text{ mVs}^{-1}$ , from  $3 \text{ V}$  to upper cut-off voltages from  $4.1 \text{ V}$  to  $5.5 \text{ V}$  in  $0.1 \text{ V}$  steps, at  $60^\circ\text{C}$ ) in SST||Li metal cells.

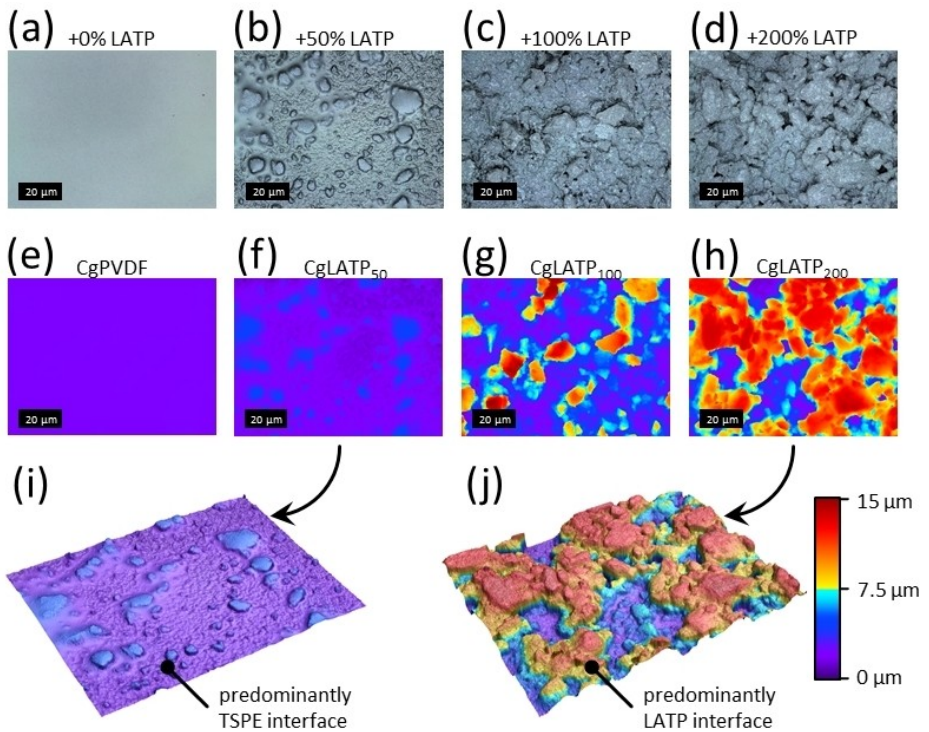


**Figure 5.** Influence of the LATP-loading in the cathode layer of multi-layer electrolytes on the surface properties. (a) Combined optical and laser image of (a) CgPVDF, (b) CgLATP<sub>50</sub>, (c) CgLATP<sub>100</sub>, (d) CgLATP<sub>200</sub>; surface topography of (e) CgPVDF, (f) CgLATP<sub>50</sub>, (g) CgLATP<sub>100</sub>, (h) CgLATP<sub>200</sub> from 0 μm (purple) to 15 μm (dark red); (i) 3D visualization of f; (j) 3D visualization of h.

CgLATP<sub>50</sub>, a second LATP phase is visible at the interface by smaller grains of <1 μm as well as some larger agglomerates of >5 μm, see Figure 5b. As the LATP content is further increased, the interface becomes increasingly dominated by LATP agglomerates, see Figure 5c and d. The surface roughness increases with LATP addition from <0.1 μm (CgPVDF), 0.55 ± 0.09 μm (CgLATP<sub>50</sub>), 2.28 ± 0.41 μm (CgLATP<sub>100</sub>) to 2.62 ± 0.13 μm (CgLATP<sub>200</sub>), see Figure 5e to h. Comparing the 3D profile of CgLATP<sub>50</sub> to CgLATP<sub>200</sub>, the interface of CgLATP<sub>50</sub> is predominantly TSPE with the LATP particles covered and connected by TSPE, while for CgLATP<sub>200</sub> the interface is predominantly LATP with large pits and some particles not fully connected by TSPE, see Figure 5i and j.

The addition of LATP and the change of morphology directly affect the electrochemical performance of the electrolyte in a battery. Two main regions of interest have been distinguished: the bulk ionic conductivity, which represents the Li ion transport through the electrolyte, and the electrolyte|NMC622 interface and interphase (I&I), which allows the transition to and intercalation into the cathode material. Both regions must provide adequate ion transport to NMC622 for a battery application. To quantify the bulk performance, the ionic conductivity of the electrolytes is measured by impedance spectroscopy, see Figure 6a and b. To minimize the effects of poor contact on the conductivity due to a rough electrolyte interface, the electrolytes are sandwiched between two soft Li metal electrodes, providing a high surface area at both Li metal|electrolyte I&Is. The ionic conductivity increases with the addition of LATP from (0.170 ± 0.001) mS cm<sup>-1</sup> for CgPVDF to

(0.370 ± 0.002) mS cm<sup>-1</sup> for CgLATP<sub>50</sub> and reaches its maximum at (0.712 ± 0.008) mS cm<sup>-1</sup> for CgLATP<sub>100</sub>. As the fraction of highly conductive LATP increases, the overall bulk ionic conductivity enhances. For CgLATP<sub>200</sub>, however, the ionic conductivity decreases again to (0.167 ± 0.002) mS cm<sup>-1</sup>. This is explained by the percolation theory. When the LATP content exceeds a certain volume fraction, the highly conductive SIE domains are no longer properly connected, resulting in poor ion transport through the electrolyte. The temperature-dependent ionic conductivity of the electrolytes follows the Vogel-Fulcher-Tamman (VFT) behavior, which is typical for polymer-based electrolytes, see Equation 1.<sup>[18]</sup> The temperature-dependent ionic conductivity depends on the pre-exponential factor  $\sigma_0$ , the activation energy for ionic conduction  $E_A$ , the Boltzmann constant  $k_B$  and the ideal glass transition temperature  $T_0$ , also known as the Vogel temperature (about 50 K below  $T_G$ ).

$$\sigma(T) = \sigma_0 \cdot \exp \left[ \frac{-E_A}{k_B \cdot (T - T_0)} \right] \quad \begin{cases} \sigma = & \text{ionic conductivity / mS cm}^{-1} \\ \sigma_0 = & \text{pre-exponential factor / mS cm}^{-1} \\ E_A = & \text{activation energy for ionic conduction / eV} \\ k_B = & \text{Boltzmann constant / eV K}^{-1} \\ T = & \text{temperature / K} \\ T_0 = & \text{ideal glass transition temperature / K} \end{cases} \quad (1)$$

To quantify the performance of the electrolyte|NMC622 I&I, staircase voltammetry coupled with impedance spectroscopy is applied to NMC622||Li metal cells. The upper cut-off voltage is increased in 0.025 V steps from 3.8 V to 4.50 V. To minimize the effect of overvoltage on the capacity utilization of the cathode material a low current of 0.05 mA cm<sup>-2</sup> is applied. The specific capacity of the cycle with a cut-off voltage of 4.25 V is shown in

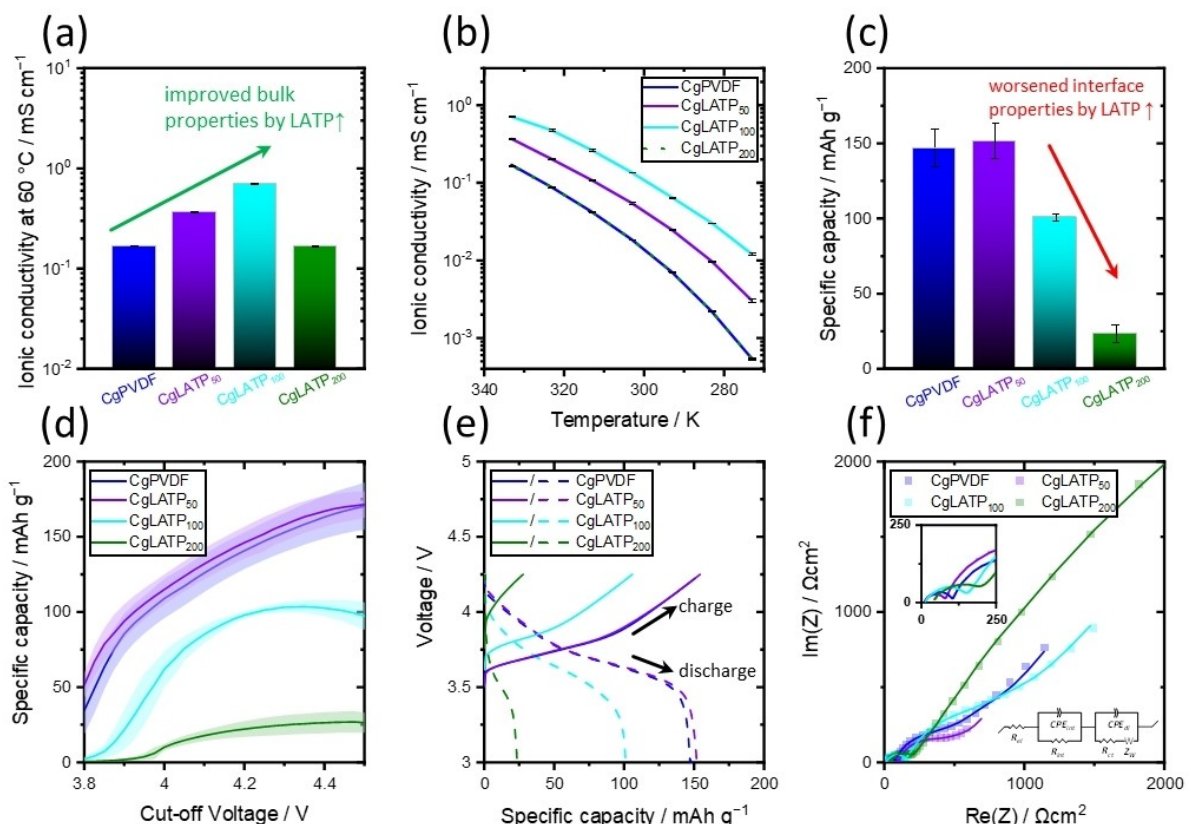


**Figure 6.** Impact of LATP content on bulk and interfacial properties. (a) Ionic conductivity taken from b measured at 60 °C in Li||Li cells by impedance spectroscopy; (b) ionic conductivity versus temperature from 0 °C to 60 °C in Li||Li cells by impedance spectroscopy, inset shows the Nyquist plots at 60 °C; (c) specific capacity taken from d with 0.05 mA cm<sup>-2</sup> and cut-off voltages of 3.00 V – 4.25 V in NMC622||Li cells; (d) specific capacity versus applied cut-off voltage of a staircase voltammetry in NMC622||Li cells with an applied lower cut-off voltage of 3.00 V and an ever increasing upper cut-off voltage from 3.80 V to 4.50 V in 0.025 V steps and a current of 0.05 mA cm<sup>-2</sup>; (e) voltage profiles of a charge/discharge profile of d with a cut-off voltage of 3.00 V to 4.25 V; impedance spectroscopy measurement after the first cycle of d, inset shows the applied equivalent circuit used to fit the data and the high frequency region.

Figure 6c. The highest specific capacities are achieved for CgPVDF of  $(147 \pm 13)$  mAh g<sup>-1</sup> and for CgLATP<sub>50</sub> of  $(152 \pm 11)$  mAh g<sup>-1</sup>, which agrees with the morphological analysis showing a predominantly TSPE interface well suited for the NMC622 cathode contact. With increasing LATP content, the specific capacity decreases for CgLATP<sub>100</sub> to  $(101 \pm 2)$  mAh g<sup>-1</sup> and for CgLATP<sub>200</sub> to  $(23 \pm 6)$  mAh g<sup>-1</sup>. As the rough LATP interface dominates in these samples, the contact area to NMC622 decreases, resulting in a reduced capacity utilization, see Figure 6d. An increasing specific capacity is noticeable for CgPVDF and CgLATP<sub>50</sub>, reaching a value of about 171 mAh g<sup>-1</sup> at a cut-off voltage of 4.5 V. For CgLATP<sub>100</sub>, a drop of the specific capacity occurs from 4.35 V, possibly due to a loss of contact during cycling by the volume changes of the cathode active material. A contact area smaller than the projected surface area of the electrolyte|NMC622 I&I also results in a higher overvoltage as the Li<sup>+</sup> flux is concentrated on small regions, see Figure 6e. The overvoltage increases from CgLATP<sub>50</sub> to CgLATP<sub>100</sub> and is the highest for CgLATP<sub>200</sub>.

Finally, impedance spectroscopy was used to further understand the contact region of the electrolyte|NMC622 I&I. The Nyquist plots measured after the first cycle are shown in Figure 6f. A  $R_{el} + (R_{int}/CPE_{int}) + (CPE_{dl}/R_{ct}) + Z_W$  circuit is used to fit the data, see lower inset in Figure 6f. The elements resistor ( $R$ ),

constant phase element (CPE), and a transport (Warburg) element ( $Z_W$ ) are used. Three sections connected in series are applied to represent the full cell. The bulk electrolyte resistance in the high frequency region is represented by  $R_{el}$ . The electrode|electrolyte I&I is represented by the I&I resistance ( $R_{int}$ ) and the capacitor-like behaviour of the ionic double layer ( $CPE_{int}$ ). The slow electrochemical processes in the low frequency region, such as charge transfer to and within the NMC622 particles and the ion transport in the electrolyte, are represented by a  $CPE_{dl}/R_{ct} + Z_W$  element. These processes are represented by the charge transfer resistance at the electrolyte|NMC622 I&I ( $R_{ct}$ ), the capacitor-like behavior of the ionic double layer at the electrolyte|NMC622 I&I ( $CPE_{dl}$ ), and a Warburg transport element for ion diffusion ( $Z_W$ ).  $R_{ct}$  depends on the resistance for charge transfer and the contact area at the electrolyte|NMC622 I&I. Additionally,  $R_{ct}$  is influenced by the state of charge (SOC) of the cathode, so the impedances after the first discharge are observed for all cells.<sup>[48,49]</sup> A high  $R_{ct}$  indicates a poor contact resulting in low capacity utilization of the cathode material. The fitted  $R_{ct}$  values agree with the specific capacities and the morphological data as low values are achieved for CgPVDF ( $398 \Omega \text{cm}^2$ ) and CgLATP<sub>50</sub> ( $360 \Omega \text{cm}^2$ ), and high values, and therefore a low contact area, are present in CgLATP<sub>100</sub> ( $784 \Omega \text{cm}^2$ ) and CgLATP<sub>200</sub> ( $13,511 \Omega \text{cm}^2$ ).

In summary, CgLATP<sub>50</sub> is the best compromise to balance bulk ionic conductivity and interfacial properties, as the highest specific capacity is achieved with CgLATP<sub>50</sub> in NMC622||Li cells and also the bulk ionic conductivity is improved by the LATP addition.

### Impact of the ionic liquid on phase behavior

The advantage of the IL is that it interconnects the phases of the multi-layer electrolyte, resulting in high ionic conductivity through the electrolyte. Therefore, in this section, the compatibility of the IL with the other electrolyte materials and the phase behavior of the mixture are elaborated. To achieve high performance, the ions in the electrolyte should be highly mobile. However, when a Li salt is added to Pyr<sub>14</sub>TFSI, the Li ion mobility is reduced by the formation of  $[\text{Li}(\text{TFSI})_n]^{(n-1)-}$  complexes.<sup>[50–53]</sup> As shown by Raman measurements, the formation of such ion clusters depends most importantly on the ratio of Pyr<sub>14</sub>TFSI to LiTFSI, see Figure 7a. The signal of free TFSI<sup>-</sup> at  $\sim 740 \text{ cm}^{-1}$  increases with Pyr<sub>14</sub>TFSI content in relation to that of coordinated TFSI<sup>-</sup> at  $\sim 748 \text{ cm}^{-1}$ . Therefore, a valid strategy to increase Li ion mobility is to raise the Pyr<sub>14</sub>TFSI content (CgLATP<sub>50</sub>  $\rightarrow$  CgLATP<sub>50</sub> +). The effects on performance are further elaborated by measuring the exchange current density ( $j_{\text{ex}}$ ) and

the limiting current density ( $j_{\text{lum}}$ ) as described by Wetjen *et al.*, see SI Table 1.<sup>[54]</sup> Furthermore, the polymers and SIEs will also affect the ion dissociation, see Figure 7b. For CgLATP<sub>50</sub>, the PEO-TSPE anode phase and the LATP<sub>50</sub> cathode phase are analyzed by Raman spectroscopy. In both phases only free TFSI<sup>-</sup> is detected, indicating a strong interaction of the ions with the solid matrices. According to the literature, the nature of this interaction varies for PEO, PVDF-HFP, and LATP. PEO is known to be able to dissolve LiTFSI by coordination of the oxygen atoms of the ethylene oxide groups to the Li ions.<sup>[18,55]</sup> Fluorinated polymers such as PVDF (8.3) have a higher relative permittivity than PEO (5), but the solubility of LiTFSI is still limited because there are no oxygen coordinating groups in the structure.<sup>[18,56]</sup> Therefore, the interaction between a Li salt and PVDF-HFP is highly dependent on the anion of the salt. Cznotka *et al.* used the term of fluorophilicity of the anion to evaluate the interaction with PVDF-HFP.<sup>[57]</sup> The higher the fluorine content in the anion, the stronger the interaction with the polymer matrix. For LATP, the surface groups of the particles contribute to ion dissociation by Lewis acid-base interactions with the Li salt and IL.<sup>[14,58]</sup>

The compatibility of the liquid Pyr<sub>14</sub>TFSI phase with the solid PEO, LATP and PVDF-HFP phases is further evaluated by contact angle ( $\theta$ ) measurements. The basis for this is the placement of a liquid Pyr<sub>14</sub>TFSI drop on the solid films, which are cast and dried

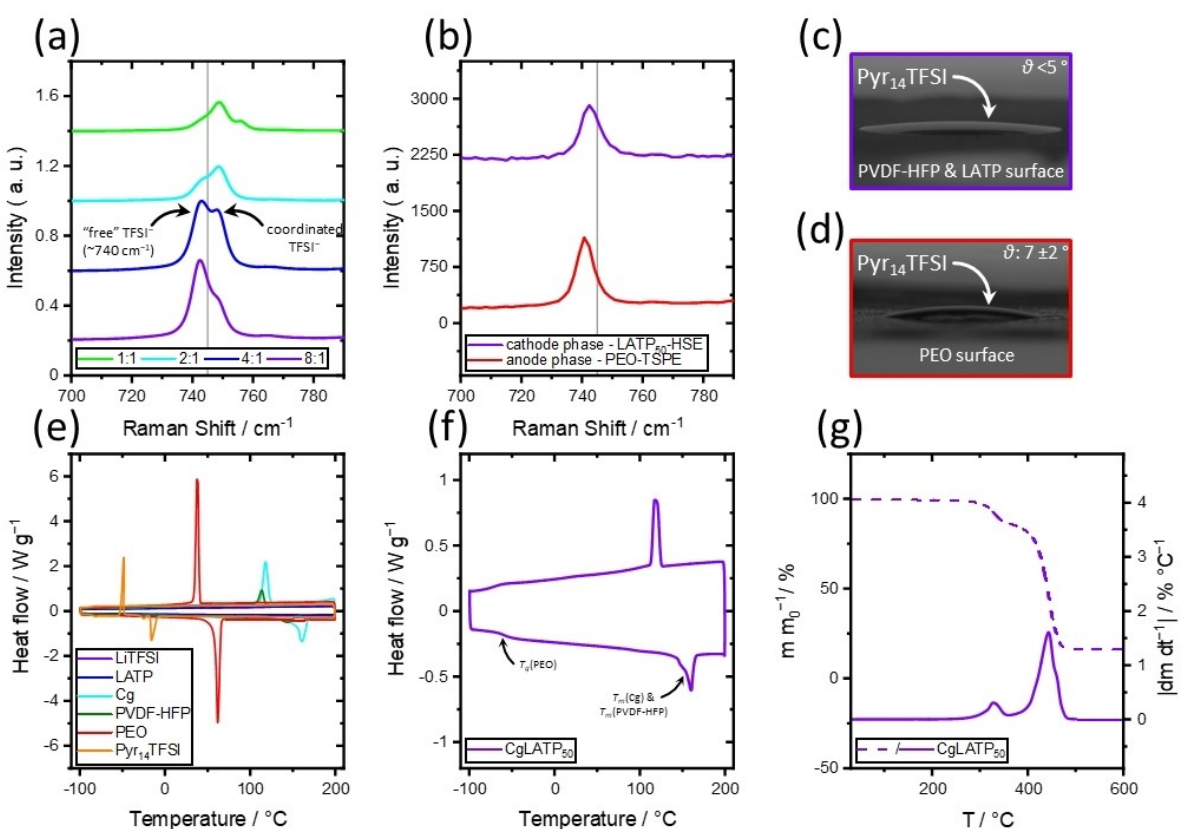


**Figure 7.** Impact of Pyr<sub>14</sub>TFSI on the phase behavior of the electrolyte. (a) Raman measurements of Pyr<sub>14</sub>TFSI:LiTFSI mixtures with different mole ratios of 1:1, 2:1, 4:1, and 8:1; (b) solid-state Raman measurement of the cathode and anode phase of CgLATP<sub>50</sub>; (c) contact angle measurement of Pyr<sub>14</sub>TFSI on a  $\sim 50 \mu\text{m}$  thick cast and dried PVDF-HFP:LATP film of a 1:1 mass ratio; (d) contact angle measurement of Pyr<sub>14</sub>TFSI on a  $\sim 50 \mu\text{m}$  thick casted and dried PEO film; (e) DSC measurement of LiTFSI, LATP, Cg, PVDF-HFP, PEO, and Pyr<sub>14</sub>TFSI from  $-100^\circ\text{C}$  to  $200^\circ\text{C}$  at a heating rate of  $10 \text{ K min}^{-1}$ ; (f) DSC measurement of CgLATP<sub>50</sub> from  $-100^\circ\text{C}$  to  $200^\circ\text{C}$  at a heating rate of  $10 \text{ K min}^{-1}$ ; (g) TGA measurement of CgLATP<sub>50</sub> from  $30^\circ\text{C}$  to  $600^\circ\text{C}$  at a heating rate of  $10 \text{ K min}^{-1}$ .

PEO and PVDF-HFP & LATP (50:50) films, see Figure 7c and d. A  $\theta < 90^\circ$  indicates a strong affinity/compatibility of the liquid and solid phases to each other, while a  $\theta > 90^\circ$  indicates a poor wetting behavior because of different phase polarities. In both cases, a  $\theta \ll 90^\circ$  is measured, demonstrating a high compatibility of the materials due to strong interaction. A high affinity of the Pyr<sub>14</sub>TFSI to the solids is necessary to avoid phase separation and to maintain the solid character of the electrolyte by IL uptake. The  $\theta$  value is described by Young's equation, where the Young's contact angle ( $\theta_y$ ) is determined by the three interfacial energies ( $\gamma_{sg}$ ,  $\gamma_{sl}$ ,  $\gamma_{lg}$ ) between the three phases solid (s), liquid (l) and gas (g), see Equation 2.<sup>[59]</sup> Young's equation describes the system in thermodynamic equilibrium. This is not the case for the presented system shown in Figure 7c and d as the  $\theta$  does not remain stable but shows a continuous wetting over time, compare SI Figure 5. Nevertheless, the advance of  $\theta \ll 90^\circ$  indicates a clear tendency of compatibility of the two phases.

$$\begin{aligned} \gamma_{sg} &= \text{interfacial energy solid-gas / J m}^{-2} \\ \gamma_{sl} &= \text{interfacial energy solid-liquid / J m}^{-2} \\ \gamma_{lg} &= \text{interfacial energy liquid-gas / J m}^{-2} \\ \theta_y &= \text{Young's contact angle / }^\circ \end{aligned} \quad (2)$$

The lower value measured for the PVDF-HFP & LATP film ( $< 5^\circ$ ) compared to PEO ( $< 7 \pm 2^\circ$ ) is attributed to the high surface roughness of the LATP particles in contrast to the flat PEO film. As described by Wenzel's equation the measured Wenzel's contact angle ( $\theta_w$ ) is  $< \theta_y$ . Due to the roughness, the actual solid-liquid surface area ( $A_{sl}$ ) is greater than the assumed projected surface area ( $A_{projected}$ ), thereby reducing the  $\theta$ .<sup>[59]</sup>

$$\cos \theta_w = \frac{A_{sl}}{A_{projected}} \cdot \cos \theta_y \quad \begin{aligned} A_{sl} &= \text{solid-liquid surface area / m}^2 \\ A_{projected} &= \text{projected surface area / m}^2 \\ \theta_w &= \text{Wenzel's contact angle / }^\circ \\ \theta_y &= \text{Young's contact angle / }^\circ \end{aligned} \quad (3)$$

The interaction between the phases and the degree of disorder is further evaluated by comparing the DSC measurement of the pure educts with CgLATP<sub>50</sub>, compare Figure 7e and f. In addition, the DSC measurements of the pure educts are shown separately in SI Figure 3. For pure PEO, the melting point ( $T_m$ ) of the crystalline phase is at approximately 60 °C and the glass transition ( $T_g$ ) is at -54 °C. In the electrolytes, the  $T_m$  is not visible, indicating a fully amorphous state, which increases the polymer chain mobility and favors fast ion transport through the electrolyte. Instead, only a glass transition ( $T_g$ ) for PEO is visible in CgLATP<sub>50</sub> at about -62 °C. For LATP and LiTFSI no phase transitions are visible in the set temperature range. For Pyr<sub>14</sub>TFSI two main signals are visible from -8 °C, a recrystallization peak at -48 °C and a  $T_g$  at ~-81 °C, in agreement with other literature results.<sup>[60]</sup> These signals are not present in CgLATP<sub>50</sub>, indicating a strong interaction with the SE matrix. For Cg, a  $T_m$  of 160 °C is observed for pure Cg and in the electrolyte, indicating that the separator does not dissolve from the components and remains solid at the operating temperature. For pure PVDF-HFP, a  $T_m$  of 143 °C is observed, which is in the same range as  $T_m$ (Cg). For CgLATP<sub>50</sub>, aside shoulder is observed

at the  $T_m$ (Cg) signal, indicating that PVDF-HFP may not be fully plasticized by Pyr<sub>14</sub>TFSI. Overall, the DSC of CgLATP<sub>50</sub> compared to the pure educts shows a disappearance of several  $T_m$ s and a shift in  $T_g$ s highlighting the strong plastification effect of the IL on the components.

The TGA of CgLATP<sub>50</sub> shows an overall high thermal stability of  $\geq 250$  °C, see Figure 7g. Therefore, in contrast to gel polymer electrolytes (GPEs) in which organic solvents with boiling points commonly  $< 100$  °C are applied as plasticizers, the IL maintains the high thermal stability of the SE due to its neglectable vapour pressure. In summary, the IL has a good compatibility to the other components enabling a high degree of plastification and disorder, which governs a high ion conduction. A high thermal stability of the CgLATP<sub>50</sub> is enabled, and the Pyr<sub>14</sub>TFSI content can be increased to enhance performance of the electrolyte.

### Impact of the Cg on the bulk electrolyte properties

Cg is a microporous flexible polymer film, see Figure 8a. Its typical MD (machine direction) tensile strength of 1170 kg cm<sup>-2</sup> (manufacturer's specification) stabilizes the thin CgLATP<sub>50</sub> + films compared to elastic, mechanically weak HSE/TSPE films.<sup>[41,61,62]</sup> This allows for an overall thin electrolyte film ( $\leq 50$  µm) and for high gravimetric/volumetric densities without sacrificing its applicability, see Figure 8b.<sup>[55]</sup> Furthermore, as Cg is already commercially applied, its mechanical strength allows CgLATP<sub>50</sub> + more easily being processed with current Li ion battery cell manufacturing technology, which requires the film to be wound with high forces and easily stacked in the cell set-up.<sup>[4]</sup> Further still, the mechanical strength inhibits dendrite penetration through the electrolyte when operated against Li metal at high areal capacities.<sup>[41]</sup>

Commonly used cathode materials require an areal capacity of  $\leq 5$  mAh cm<sup>-2</sup>, which is matched by the CgLATP<sub>50</sub> + electrolyte with an areal capacity utilization of  $> 20$  mAh cm<sup>-2</sup>, see Figure 8c. The areal capacity utilization is determined by sandwiching the electrolyte between two Li metal electrodes and operating it with a galvanostatic single discharge measurement ("short-circuit measurement") at a specified current density until the cell fails by short-circuiting. The areal capacities of seven individual cells at different current densities from 0.1 mA cm<sup>-2</sup> to 0.4 mA cm<sup>-2</sup> are plotted against the areal capacity until short-circuit, see Figure 8c. In general, higher capacity utilization is achieved at lower current densities. High currents can increase the likelihood of Li metal penetrating the electrolyte, e.g. by dendrite formation.<sup>[63]</sup> In general, the areal capacity utilization of CgLATP<sub>50</sub> + is higher compared to pure polymer-based SEs, such as TSPEs, which can suffer from short-circuit due to their soft polymer-IL matrix.<sup>[41,62]</sup>

Furthermore, the porous structure acts as a physical barrier to keep the LATP on the cathode side. As seen from the FT-IR spectra obtained from both sides of the CgLATP<sub>50</sub> + electrolyte, the broad LATP band from 1200 cm<sup>-1</sup> to 800 cm<sup>-1</sup> due to the symmetric stretching of PO<sub>4</sub><sup>3-</sup> is present only at the cathode side, see Figure 8d. Additionally, there is no evidence of mixing

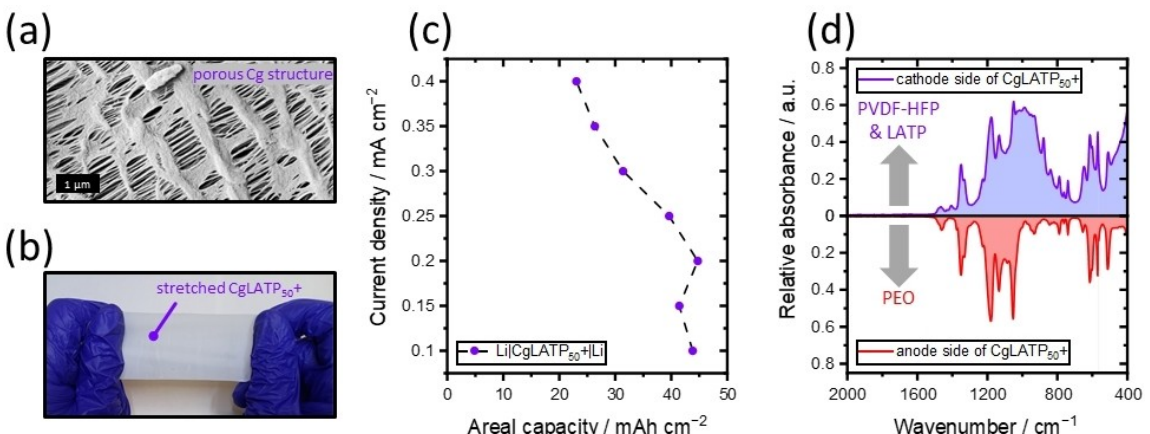


**Figure 8.** Impact of the Cg on processability, dendrite prevention and phase separation. (a) SEM image of the porous structure of Cg; (b) top view of a stretched CgLATP<sub>50+</sub> film; (c) galvanostatic single discharge polarization of Li||Li cells at currents from 0.1 mAh cm<sup>-2</sup> to 0.4 mAh cm<sup>-2</sup> at 60 °C

of the polymers, maintaining two phases. Note that the symmetric CH<sub>2</sub> stretching of PVDF-HFP (1406 cm<sup>-1</sup>) is only present on the cathode side, while for the anode side the CH<sub>2</sub> scissoring signal (1461 cm<sup>-1</sup>) is much higher than on the cathode side, because not only Pyr<sub>14</sub>TFSI but also PEO contributes to it.<sup>[64–66]</sup> In summary, the porous and mechanically strong Cg layer benefits the application in current battery manufacturing techniques, prevents short-circuits and separates the two electrolyte phases.

#### Impact of the anode-facing electrolyte on Li metal compatibility

For the anode side of the multi-layer HSE, the ESW<sub>lower</sub> and the ability to contact Li metal during electro-deposition/-dissolution determine the suitability of electrolyte materials. As will be shown, PEO is a better alternative than PVDF-HFP and LATP. In LATP, the Ti<sup>4+</sup> is reduced by Li metal to Ti<sup>3+</sup>, resulting in the formation of various degradation products such as oxides, titanates, phosphides, phosphates and aluminum oxides.<sup>[67,68]</sup> These are low in ionic conductivity and reduce the performance of the electrolyte. Therefore, LATP is added only to the cathode side of the electrolyte. As shown in a previous publication, PVDF-HFP-based electrolytes (0.1 mS cm<sup>-1</sup>) have lower ionic conductivity at 60 °C and  $j_{lim}$  than PEO-based electrolytes (0.4 mS cm<sup>-1</sup>).<sup>[42]</sup> Furthermore, PVDF-HFP is a stiffer polymer compared to PEO and is less able to swell upon liquid uptake, resulting in a much harder surface that is less able to maintain contact with the Li metal. To demonstrate the difference in Li metal contact ability, a CgPVDF electrolyte (one side PEO-TSPE, other side PVDF-HFP-TSPE) is sandwiched between two Li metal electrodes and a staircase galvanostatic polarization measurement is performed. The current density is increased from 0.05 mA cm<sup>-2</sup> in 0.05 mA cm<sup>-2</sup> increments and the voltage profile is monitored. Since the step time is kept constant, the cycled capacity also increases with increasing current density. A positive voltage corresponds to Li metal electro-dissolution from the PEO side and a negative voltage corresponds to Li

metal electro-dissolution from the PVDF-HFP side. From 0.15 mA cm<sup>-2</sup>, electro-dissolution from the PVDF-HFP side leads in an increasing voltage profile, which may be related to contact loss due to pitting or an insufficient Li ion transport in the layer, while the voltage profile from the electro-dissolution of the PEO side remains stable.<sup>[69]</sup> From 0.20 mA cm<sup>-2</sup>, the voltage profile of electro-dissolution Li metal from the PVDF-HFP side runs into the cut-off voltage, showing PEO is the better option for Li metal contact. It should also be noted that PEO is stable to Li metal while PVDF-HFP degrades.<sup>[7]</sup> During anodic decomposition, the highly electronegative fluorine groups of PVDF-HFP react with the reductive Li metal to form lithium fluorite (LiF).<sup>[70]</sup> However, since the LiF in the SEI is considered to be stable and low in resistance, the contacting ability of the two TSPEs discussed are more critical in this case than the ESW<sub>lower</sub>.<sup>[70,71]</sup>

To demonstrate a reversible Li metal electro-deposition/-dissolution, two CgLATP<sub>50+</sub> electrolyte films are sandwiched in an ABBA fashion. The two PEO sides are facing outwards and the electrolyte sandwich is placed between two Li metal electrodes. Galvanostatic polarization measurement is applied at 0.1 mA cm<sup>-2</sup> for 0.5 mAh cm<sup>-2</sup>. During the first 100 h, the voltage curve decreases due to the electro-deposition of "fresh" Li metal on the Li metal anode covered with the resistive artificial SEI.<sup>[72,73]</sup> A small voltage increase of 0.011 V is observed from 100 h to 1,000 h, reflecting a minimal effect of resistances accumulated over the cycle duration, which could be attributed to the formation of dead lithium. The Li metal electrode-deposition is analyzed in Cu||Li cells. 2 mAh cm<sup>-2</sup> of Li metal is deposited on the flat copper surface by applying a current of 0.05 mA cm<sup>-2</sup>. As shown in Figure 9c, Li grains of about  $\leq 20 \mu\text{m}$  are deposited homogeneously in a mosaic-like fashion without any empty spaces. The surface height profile of the Li deposit is further elaborated in Figure 9d. The overall electro-deposition is homogeneous since the maximal height difference is  $< 2 \mu\text{m}$  with a slight deepening at the grain boundaries. The homogeneity is maintained at different current densities and Li metal grain sizes, compare SI Figure 6. The uniform Li metal distribution could be attributed to a synergistic effect of great contact

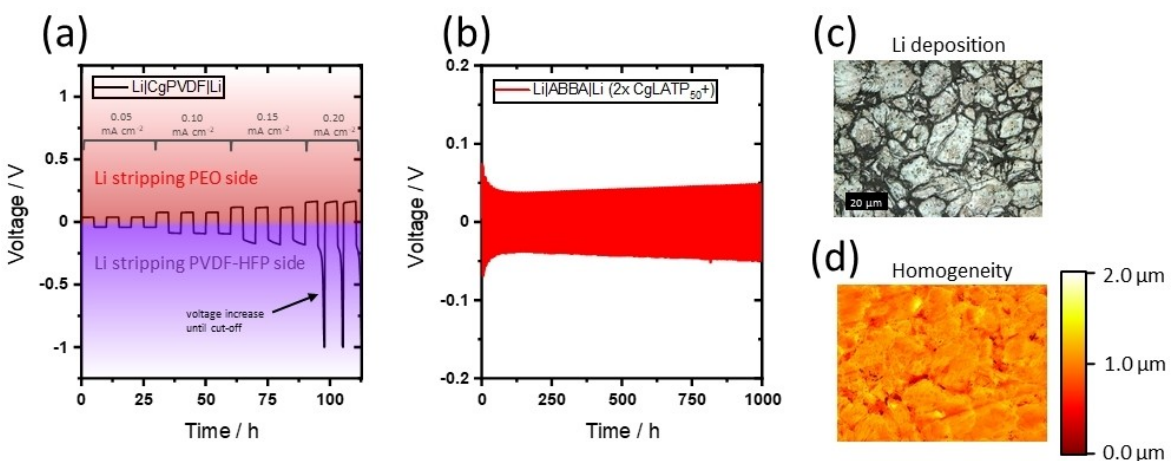


**Figure 9.** Impact of the anode-facing layer. (a) Staircase galvanostatic polarization measurement (from  $0.05 \text{ mA cm}^{-2}$ ,  $0.5 \text{ mAh cm}^{-2}$ , increase by  $0.05 \text{ mA cm}^{-2}$  every 3 cycles,  $60^\circ\text{C}$ ) with  $\text{Li metal}||\text{Li metal}$  cells; (b) galvanostatic polarization measurement ( $0.1 \text{ mA cm}^{-2}$ ,  $0.5 \text{ mAh cm}^{-2}$ , 1,000 h, two electrolyte films in ABBA arrangement) with  $\text{Li metal}||\text{Li metal}$  cells; (c) LSM image of a copper surface after galvanostatic single charge electro-deposition ( $0.05 \text{ mA cm}^{-2}$ ,  $2.0 \text{ mAh cm}^{-2}$ ,) with  $\text{Cu}||\text{Li metal}$  cells; (d) topography of image c.

provided by the soft PEO-TSPE layer to the electrode interface and an ion flow homogenizing effect of the highly tortuous and mechanically rigid Cg layer. In summary, the PEO-TSPE layer of the  $\text{CgLATP}_{50+}$  enables stable Li metal cycling and a homogeneous Li electro-deposition.

### Cycling Performance

The long-term cycling performance of the  $\text{CgLATP}_{50+}$  electrolyte is determined in two systems of LFP||Li metal cells and

NMC622||Li metal cells, see Figure 10. LFP is a commonly used cathode material in all solid-state batteries (SSBs) because it is highly stable during cycling and requires less oxidative stability from the SEs, being a 3 V cathode material. It also attracted attention for its lower environmental impact compared to NMC-based cathodes.<sup>[74]</sup> NMC622 is a cathode material of the 4 V category and is less commonly used in SSBs, but promises a higher energy density compared to LFP.

In the 1<sup>st</sup> cycle LFP||Li metal cells show an increased overvoltage compared to the following cycles due to the aforementioned effects of the resistance from the artificial SEI

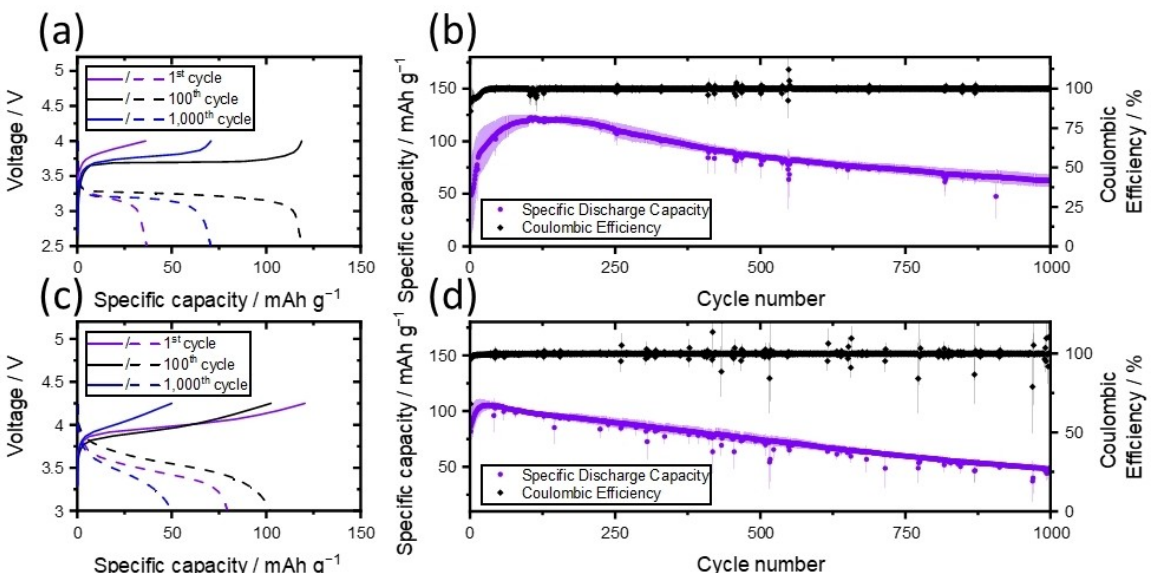


**Figure 10.** Long-term cycling of LFP||Li metal cells with  $\text{CgLATP}_{50+}$  at  $60^\circ\text{C}$  with  $0.2 \text{ mA cm}^{-2}$  ( $1/3 \text{ C}$ ) and cut-off voltages from  $2.50 \text{ V}$ – $4.00 \text{ V}$  and long-term cycling of NMC622||Li metal cells with  $\text{CgLATP}_{50+}$  at  $60^\circ\text{C}$  with  $0.3 \text{ mA cm}^{-2}$  ( $1/2 \text{ C}$ ) and cut-off voltages from  $3.00 \text{ V}$ – $4.25 \text{ V}$ . (a) Voltage profile over specific capacity of a LFP||Li metal cell of the 1<sup>st</sup>, 100<sup>th</sup>, and 1,000<sup>th</sup> cycle with discharge curves shown as dashed lines and charge curves shown as solid lines; (b) average specific discharge capacity and Coulombic efficiency over cycle number of LFP||Li metal cells; (c) voltage profile over specific capacity of a NMC622||Li metal cell of the 1<sup>st</sup>, 100<sup>th</sup>, and 1,000<sup>th</sup> cycle with discharge curves shown as solid lines and charge curves shown as dashed lines; (d) average specific capacity and Coulombic efficiency over cycle number of NMC622||Li metal cells.

and the deposition of "fresh" HSAL on the Li metal surface, see Figure 10a. The Coulombic efficiency is 85.81% in the 1<sup>st</sup> cycle and increases sharply in the following cycles to an average of 99.90% from the 100<sup>th</sup> to the 1,000<sup>th</sup> cycle. The capacity retention is 51.67% after 1,000 cycles, when compared to the maximum specific capacity of 120.97 mAh g<sup>-1</sup> at the 106<sup>th</sup> cycle.

The 1<sup>st</sup> cycle in NMC622||Li metal cells shows an increased overvoltage compared to the 100<sup>th</sup> cycle. The Coulombic efficiency is 68.13% in the 1<sup>st</sup> cycle and increases sharply in the following cycles to an average value of 99.86% from the 100<sup>th</sup> to the 1,000<sup>th</sup> cycle. The capacity retention is 46.06% after 1,000 cycles, when compared to the maximum specific capacity of 105.31 mAh g<sup>-1</sup> at the 31<sup>st</sup> cycle. The lower capacity retention of the NMC622||Li metal cells compared to the LFP||Li metal cells can be explained by the steady charge and discharge voltage profiles of NMC622 in contrast to the flat charge and discharge voltage profiles of the LFP and therefore a lower capacity utilization with increasing overvoltage over the number of cycles, compare Figure 10a and c.

To put the results in a larger context, the capacity retention of the NMC622||Li and LFP||Li cells is compared to other recent electrolyte systems from the literature, see Figure 11 and SI Table 2.<sup>[16,38,40,62,71,75–98]</sup> Due to the variety of materials used, electrolytes are categorized as CPIEs, TSPEs, HSEs, and SPEs. To allow for a comparison over a broad spectrum of cycle counts, the capacity retention of this work is shown in 100 cycle increments from the 100<sup>th</sup> to the 500<sup>th</sup> cycle. The capacity retention of LFP||Li metal cells with CgLATP<sub>50</sub>+ electrolyte is 98.88% (100<sup>th</sup> cycle), 97.42% (200<sup>th</sup> cycle), 86.85% (300<sup>th</sup> cycle), 77.75% (400<sup>th</sup> cycle), and 69.91% (500<sup>th</sup> cycle). The capacity retentions are in the upper range compared to the electrolytes shown in the literature. The capacity retention of NMC622||Li metal cells with CgLATP<sub>50</sub>+ electrolyte is 93.79% (100<sup>th</sup> cycle), 88.15% (200<sup>th</sup> cycle), 82.53% (300<sup>th</sup> cycle), 76.11% (400<sup>th</sup> cycle),

and 70.61% (500<sup>th</sup> cycle). The capacity retention is higher compared to the shown electrolytes from literature. In summary, the multi-layer approach of CgLATP<sub>50</sub>+ shows high capacity retention over a long cycle life. Especially when applied in NMC622||Li metal cells, the advantage of specifically designed layers shows a high impact compared to other systems.

## Conclusions

Here we report on a multi-layer HSE based on a commercially available Cg separator. A practical fabrication approach for the multi-layer HSE is presented by coating two different anode and cathode pastes on both sides of the Cg. Due to the Cg middle layer, the presented thin film ( $\leq 50 \mu\text{m}$ ) HSE shows high mechanical strength, which meets the requirements for high energy densities as well as applicability to manufacturing processes requiring a stable film. A PEO-based anode side of the electrolyte reversibly cycles Li metal and a LATP-based cathode side provides a high oxidative stability ( $\geq 4.5 \text{ V}$ ) to the cathode. As shown, a high thermal stability of  $> 250^\circ\text{C}$  and a short-circuit free cycling enables a safe operation. Long term cycling stability was achieved in NMC622||Li metal cells with a capacity retention of 88.15% after 200 cycles and 46.06% after 1,000 cycles with a Coulombic efficiency of 99.86%.

## Author Contributions

Lukas Herbers<sup>A</sup> performed the synthesis of electrolytes, cell assembly, electrochemical measurements, contact angle measurement, and evaluation of data. William Fettkether<sup>B</sup> and Lukas Herbers<sup>A</sup> performed the LSM measurements. The SEM measurements and Raman measurements were performed by Silvan Stuckenbergs<sup>A</sup>. The TGA and DSC measurements were performed by Debbie Berghus<sup>A</sup>. Martin Winter<sup>A,C</sup> and Peter Bieker<sup>C</sup> supervised the work. Lukas Herbers<sup>A</sup> wrote the first version of the manuscript, which was supplemented through contributions of Peter Bieker<sup>B</sup>, William Fettkether<sup>B</sup>, Steve W. Martin<sup>B</sup>, and Martin Winter<sup>A,C</sup>.

## Acknowledgements

The authors thank the Ministry for Culture and Science of North Rhine Westphalia (Germany) for funding this work within the International Graduate School for Battery Chemistry, Characterization, Analysis, Recycling and Application (BACCARA). Open Access funding enabled and organized by Projekt DEAL.

## Conflict of Interests

The authors declare no conflict of interest.

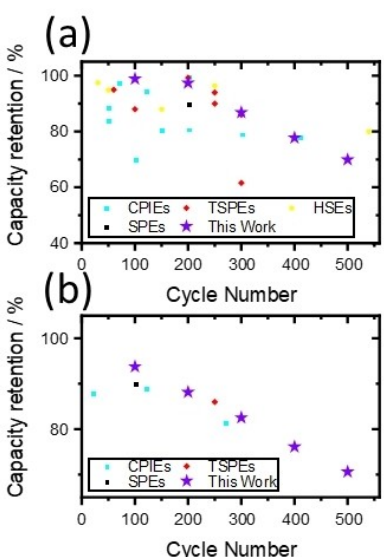


**Figure 11.** The capacity retention of various CPIEs, TSPEs, HEs, and SPEs in comparison to this work. (a) Capacity retentions in LFP||Li metal cells; (b) capacity retentions in NMC622||Li metal cells.

## Data Availability Statement

The data that support the findings of this study are available from the corresponding author upon reasonable request.

- [1] D. Lin, Y. Liu, Y. Cui, *Nat. Nanotechnol.* **2017**, *12*, 194–206.
- [2] W. Z. Wu, K. Sun, Z. Wang, *Batteries* **2022**, *8*, 246.
- [3] J. Liu, Z. Bao, Y. Cui, E. J. Dufek, J. B. Goodenough, P. Khalifah, Q. Li, B. Y. Liaw, P. Liu, A. Manthiram et al., *Nat. Energy* **2019**, *4*, 180–186.
- [4] J. W. Choi, D. Aurbach, *Nat. Rev. Mater.* **2016**, *1*.
- [5] Y. An, X. Han, Y. Liu, A. Azhar, J. Na, A. K. Nanjundan, S. Wang, J. Yu, Y. Yamauchi, *Small* **2022**, *18*, e2103617.
- [6] A. Ahniyaz, I. de Meatza, A. Kvasha, O. Garcia-Calvo, I. Ahmed, M. F. Sgroi, M. Giuliano, M. Dotoli, M.-A. Dumitrescu, M. Jahn, N. Zhang, *Adv. Appl. Energy* **2021**, *4*, 100070.
- [7] M. A. Cabañero Martínez, N. Boaretto, A. J. Naylor, F. Alcaide, G. D. Salian, F. Palombarini, E. Ayerbe, M. Borras, M. Casas-Cabanas, *Adv. Energy Mater.* **2022**, *12*, 2201264.
- [8] J. Janek, W. G. Zeier, *Nat. Energy* **2016**, *1*.
- [9] P. V. Chombo, Y. Laoouonal, *J. Power Sources* **2020**, *478*, 228649.
- [10] H. Yang, N. Wu, *Energy Sci. Eng.* **2022**, *10*, 1643–1671.
- [11] G. Yang, Y. Song, Q. Wang, L. Zhang, L. Deng, *Mater. Des.* **2020**, *190*, 108563.
- [12] N. Meng, X. Zhu, F. Lian, *Particuology* **2022**, *60*, 14–36.
- [13] X. Ji, Y. Zhang, M. Cao, Q. Gu, H. Wang, J. Yu, Z.-H. Guo, X. Zhou, *J. Adv. Ceram.* **2022**, *11*, 835–861.
- [14] Z. Cheng, T. Liu, B. Zhao, F. Shen, H. Jin, X. Han, *Energy Storage Mater.* **2021**, *34*, 388–416.
- [15] W. Zhou, S. Wang, Y. Li, S. Xin, A. Manthiram, J. B. Goodenough, *J. Am. Chem. Soc.* **2016**, *138*, 9385–9388.
- [16] H. Duan, M. Fan, W.-P. Chen, J.-Y. Li, P.-F. Wang, W.-P. Wang, J.-L. Shi, Y.-X. Yin, L.-J. Wan, Y.-G. Guo, *Adv. Mater.* **2019**, *31*, e1807789.
- [17] H. M. Woolley, N. M. Vargas-Barbosa, *J. Mater. Chem. A* **2023**, *11*, 1083–1097.
- [18] J. Mindemark, M. J. Lacey, T. Bowden, D. Brandell, *Prog. Polym. Sci.* **2018**, *81*, 114–143.
- [19] J. Li, F. Li, L. Zhang, H. Zhang, U. Lassi, X. Ji, *Green Chem. Eng.* **2021**, *2*, 253–265.
- [20] W. Xu, X. Liao, W. Xu, C. Sun, K. Zhao, Y. Zhao, C. Hu, *Nano Energy* **2021**, *88*, 106237.
- [21] S. Li, M. Jiang, Y. Xie, H. Xu, J. Jia, J. Li, *Adv. Mater.* **2018**, *30*, e1706375.
- [22] H. Zhang, G. G. Eshetu, X. Judez, C. Li, L. M. Rodriguez-Martinez, M. Armand, *Angew. Chem.* **2018**, *57*, 15002–15027.
- [23] D. Zhang, M. Liu, J. Ma, K. Yang, Z. Chen, K. Li, C. Zhang, Y. Wei, M. Zhou, P. Wang, Y. He, W. Lv, Q.-H. Yang, F. Kang, Y.-B. He, *Nat. Commun.* **2022**, *13*, 6966.
- [24] Y. Zhang, Y. Wu, H. Li, J. Chen, D. Lei, C. Wang, *Nat. Commun.* **2022**, *13*, 1297.
- [25] L. Chen, J. G. Connell, A. Nie, Z. Huang, K. R. Zavadil, K. C. Klavetter, Y. Yuan, S. Sharifi-Asl, R. Shahbazian-Yassar, J. A. Libera, A. U. Mane, J. W. Elam, *J. Mater. Chem. A* **2017**, *5*, 12297–12309.
- [26] F. Guo, C. Wu, H. Chen, F. Zhong, X. Ai, H. Yang, J. Qian, *Energy Storage Mater.* **2020**, *24*, 635–643.
- [27] L. Lin, F. Liang, K. Zhang, H. Mao, J. Yang, Y. Qian, *J. Mater. Chem. A* **2018**, *6*, 15859–15867.
- [28] M. L. Meyerson, P. E. Papa, A. Heller, C. B. Mullins, *ACS Nano* **2021**, *15*, 29–46.
- [29] H. Zhou, S. Yu, H. Liu, P. Liu, *J. Power Sources* **2020**, *450*, 227632.
- [30] Z. Ahaliabadeh, X. Kong, E. Fedorovskaya, T. Kallio, *J. Power Sources* **2022**, *540*, 231633.
- [31] M. Bandpey, M. Dorri, A. Babaei, C. Zamani, M. Bortolotti, *ACS Appl. Energ. Mater.* **2023**, *6*, 7974–7984.
- [32] H. Dong, Du Sun, M. Xie, M. Cai, Z. Zhang, T. Cai, W. Dong, F. Huang, *Dalton Trans.* **2022**, *51*, 12532–12539.
- [33] J. Li, Y. Ji, H. Song, S. Chen, S. Ding, B. Zhang, L. Yang, Y. Song, F. Pan, *Nano-Micro Lett.* **2022**, *14*, 191.
- [34] S. Tubtimkuna, N. Phattharasupakun, P. Bunyanidhi, M. Sawangphrak, *Adv. Mater. Technol.* **2022**, *7*, 2200436.
- [35] F. Xin, A. Goel, X. Chen, H. Zhou, J. Bai, S. Liu, F. Wang, G. Zhou, M. S. Whittingham, *Chem. Mater.* **2022**, *34*, 7858–7866.
- [36] L. Li, H. Duan, J. Li, L. Zhang, Y. Deng, G. Chen, *Adv. Energy Mater.* **2021**, *11*, 2003154.
- [37] W. Zhou, Z. Wang, Y. Pu, Y. Li, S. Xin, X. Li, J. Chen, J. B. Goodenough, *Adv. Mater.* **2019**, *31*, e1805574.
- [38] J.-Y. Liang, X.-X. Zeng, X.-D. Zhang, T.-T. Zuo, M. Yan, Y.-X. Yin, J.-L. Shi, X.-W. Wu, Y.-G. Guo, L.-J. Wan, *J. Am. Chem. Soc.* **2019**, *141*, 9165–9169.
- [39] X. Yu, J. Li, A. Manthiram, *ACS Materials Lett.* **2020**, *2*, 317–324.
- [40] H. Duan, Y.-X. Yin, Y. Shi, P.-F. Wang, X.-D. Zhang, C.-P. Yang, J.-L. Shi, R. Wen, Y.-G. Guo, L.-J. Wan, *J. Am. Chem. Soc.* **2018**, *140*, 82–85.
- [41] M. Zhang, A. L. Gui, W. Sun, J. Becking, O. Riedel, X. He, D. Berghus, V. Siozios, D. Zhou, T. Placke, M. Winter, P. Bieker, *J. Electrochem. Soc.* **2019**, *166*, A2142–A2150.
- [42] L. Herbers, J. Minář, S. Stuckenbergs, V. Küpers, D. Berghus, S. Nowak, M. Winter, P. Bieker, *Adv. Energy Sust. Res.* **2023**, *4*.
- [43] M. Montanino, M. Moreno, F. Alessandrini, G. B. Appetecchi, S. Passerini, Q. Zhou, W. A. Henderson, *Electrochim. Acta* **2012**, *60*, 163–169.
- [44] Y. Zhu, X. He, Y. Mo, *J. Mater. Chem. A* **2016**, *4*, 3253–3266.
- [45] G. B. Appetecchi, G. T. Kim, M. Montanino, F. Alessandrini, S. Passerini, *J. Electrochem. Soc.* **2006**, *153*, A1685.
- [46] G. B. Appetecchi, S. Scaccia, C. Tizzani, F. Alessandrini, S. Passerini, *J. Power Sources* **2011**, *196*, 6703–6709.
- [47] M. Ara, T. Meng, G.-A. Nazri, S. O. Salley, K. Y. Simon Ng, *J. Electrochem. Soc.* **2014**, *161*, A1969–A1975.
- [48] V. Charbonneau, A. Lasia, G. Brisard, *J. Electroanal. Chem.* **2020**, *875*, 113944.
- [49] N. Meddings, M. Heinrich, F. Overney, J.-S. Lee, V. Ruiz, E. Napolitano, S. Seitz, G. Hinds, R. Raccichini, M. Gaberšček, J. Park, *J. Power Sources* **2020**, *480*, 228742.
- [50] R.-S. Kühnel, A. Balducci, *J. Phys. Chem. C* **2014**, *118*, 5742–5748.
- [51] P. M. Bayley, G. H. Lane, L. J. Lyons, D. R. MacFarlane, M. Forsyth, *J. Phys. Chem. C* **2010**, *114*, 20569–20576.
- [52] D. R. MacFarlane, M. Forsyth, E. I. Izgorodina, A. P. Abbott, G. Annat, K. Fraser, *Phys. Chem. Chem. Phys.* **2009**, *11*, 4962–4967.
- [53] I. Nicotera, C. Oliviero, W. A. Henderson, G. B. Appetecchi, S. Passerini, *J. Phys. Chem. B* **2005**, *109*, 22814–22819.
- [54] M. Wetjen, G.-T. Kim, M. Joost, M. Winter, S. Passerini, *Electrochim. Acta* **2013**, *87*, 779–787.
- [55] J. Wu, L. Yuan, W. Zhang, Z. Li, X. Xie, Y. Huang, *Energy Environ. Sci.* **2021**, *14*, 12–36.
- [56] Y. Wu, Y. Li, Y. Wang, Q. Liu, Q. Chen, M. Chen, *J. Energy Chem.* **2022**, *64*, 62–84.
- [57] E. Cznotka, S. Jeschke, M. Grünebaum, H.-D. Wiemhöfer, *Solid State Ionics* **2016**, *292*, 45–51.
- [58] S. H. Siyal, M. Li, H. Li, J.-L. Lan, Y. Yu, X. Yang, *Appl. Surf. Sci.* **2019**, *494*, 1119–1126.
- [59] J. W. Drelich, L. Boinovich, E. Chibowski, C. Della Volpe, L. Holysz, A. Marmur, S. Siboni, *Surf. Innov.* **2020**, *8*, 3–27.
- [60] A. Martinelli, A. Matic, P. Jacobsson, L. Börjesson, A. Fericola, B. Scrosati, *J. Phys. Chem. B* **2009**, *113*, 11247–11251.
- [61] D. Zhou, M. Zhang, F. Sun, T. Arlt, J. E. Frerichs, K. Dong, J. Wang, A. Hilger, F. Wilde, M. Kolek, M. R. Hansen, P. Bieker, I. Manke, M. C. Stan, M. Winter, *Nano Energy* **2020**, *77*, 105196.
- [62] L. Herbers, V. Küpers, M. Winter, P. Bieker, *RSC Adv.* **2023**, *13*, 17947–17958.
- [63] X.-B. Cheng, R. Zhang, C.-Z. Zhao, Q. Zhang, *Chem. Rev.* **2017**, *117*, 10403–10473.
- [64] R. Gonçalves, D. Miranda, A. M. Almeida, M. M. Silva, J. M. Meseguer-Dueñas, J. G. Ribelles, S. Lanceros-Méndez, C. M. Costa, *SM&T* **2019**, *21*, e00104.
- [65] Mohamed A. Morsi, E. M. Abdelrazeq, A. M. Abdelghany, *Res. J. Pharm. Biol. Chem. Sci.* **2016**, *7*, 1877–1890.
- [66] N. Mozhzhukhina, A. Y. Tesio, L. P. M. de Leo, E. J. Calvo, *J. Electrochem. Soc.* **2017**, *164*, A518–A523.
- [67] C. Zheng, L. Li, K. Wang, C. Wang, J. Zhang, Y. Xia, H. Huang, C. Liang, Y. Gan, X. He, X. Tao, W. Zhang, *Batteries & Supercaps* **2021**, *4*, 8–38.
- [68] L. Li, Z. Zhang, L. Luo, R. You, J. Jiao, W. Huang, J. Wang, C. Li, X. Han, S. Chen, *Ionics* **2020**, *26*, 3815–3821.
- [69] Z. Jiang, Q. Han, S. Wang, H. Wang, *ChemElectroChem* **2019**, *6*, 2970–2983.
- [70] S. Qian, H. Chen, Z. Wu, D. Li, X. Liu, Y. Tang, S. Zhang, *Batteries & Supercaps* **2021**, *4*, 39–59.
- [71] A. Orue, M. Arrese-Igor, R. Cid, X. Júdez, N. Gómez, J. M. Del López Amo, W. Manalastas, M. Srinivasan, C. Rojiviriya, M. Armand, F. Agusse, P. López-Aranguren, *Journal J. Mater. Chem. A* **2022**, *10*, 2352–2361.
- [72] J. Becking, A. Gröbmeyer, M. Kolek, U. Rodehorst, S. Schulze, M. Winter, P. Bieker, M. C. Stan, *Adv. Mater. Interfaces* **2017**, *4*, 1700166.

- [73] K.-H. Chen, K. N. Wood, E. Kazyak, W. S. LePage, A. L. Davis, A. J. Sanchez, N. P. Dasgupta, *J. Mater. Chem. A* **2017**, *5*, 11671–11681.
- [74] Y. Mekonnen, A. Sundararajan, A. I. Sarwat, *SoutheastCon* **2016**, 1–6.
- [75] J. Atik, D. Diddens, J. H. Thienenkamp, G. Brunklaus, M. Winter, E. Paillard, *Angew. Chem.* **2021**, *60*, 11919–11927.
- [76] Z. Bi, S. Mu, N. Zhao, W. Sun, W. Huang, X. Guo, *Energy Storage Mater.* **2021**, *35*, 512–519.
- [77] X. Chen, W. He, L.-X. Ding, S. Wang, H. Wang, *Energy Environ. Sci.* **2019**, *12*, 938–944.
- [78] H. Erabhoina, M. Thelakkat, *Sci. Rep.* **2022**, *12*, 5454.
- [79] F. González, O. García-Calvo, P. Tiemblo, N. García, E. Fedeli, T. Thieu, I. Urdampilleta, A. Kvasha, *J. Electrochem. Soc.* **2020**, *167*, 70519.
- [80] Q. Guo, Y. Han, H. Wang, S. Xiong, W. Sun, C. Zheng, K. Xie, *J. Phys. Chem. C* **2018**, *122*, 10334–10342.
- [81] J.-P. Hoffknecht, A. Wettstein, J. Atik, C. Krause, J. Thienenkamp, G. Brunklaus, M. Winter, D. Diddens, A. Heuer, E. Paillard, *Adv. Energy Mater.* **2023**, *13*, 2202789.
- [82] J.-P. Hoffknecht, J. Atik, C. Krause, J. Thienenkamp, G. Brunklaus, M. Winter, E. Paillard, *Green Chem.* **2021**, *23*, 9935–9944.
- [83] J. Huang, Y. Huang, Z. Zhang, H. Gao, C. Li, *Energy Fuels* **2020**, *34*, 15011–15018.
- [84] H. Huo, Y. Chen, J. Luo, X. Yang, X. Guo, X. Sun, *Adv. Energy Mater.* **2019**, *9*, 1804004.
- [85] H. Huo, N. Zhao, J. Sun, F. Du, Y. Li, X. Guo, *J. Power Sources* **2017**, *372*, 1–7.
- [86] Y.-C. Jung, M.-S. Park, D.-H. Kim, M. Ue, A. Eftekhari, D.-W. Kim, *Sci. Rep.* **2017**, *7*, 17482.
- [87] J.-Y. Liang, X.-X. Zeng, X.-D. Zhang, P.-F. Wang, J.-Y. Ma, Y.-X. Yin, X.-W. Wu, Y.-G. Guo, L.-J. Wan, *J. Am. Chem. Soc.* **2018**, *140*, 6767–6770.
- [88] H. Li, Y. Du, Q. Zhang, Y. Zhao, F. Lian, *Adv. Energy Mater.* **2022**, *12*, 2103530.
- [89] Y.-J. Li, C.-Y. Fan, J.-P. Zhang, X.-L. Wu, *Dalton Trans.* **2018**, *47*, 14932–14937.
- [90] K. Liu, R. Zhang, J. Sun, M. Wu, T. Zhao, *ACS Appl. Mater. Interfaces* **2019**, *11*, 46930–46937.
- [91] F. Ma, Z. Zhang, W. Yan, X. Ma, D. Sun, Y. Jin, X. Chen, K. He, *ACS Sustainable Chem. Eng.* **2019**, *7*, 4675–4683.
- [92] I. Osada, S. M. Hosseini, S. Jeong, S. Passerini, *ChemElectroChem* **2017**, *4*, 463–467.
- [93] S. Song, Y. Wu, W. Tang, F. Deng, J. Yao, Z. Liu, R. Hu, Alamusi, Z. Wen, L. Lu, N. Hu, *ACS Sustainable Chem. Eng.* **2019**, *7*, 7163–7170.
- [94] X. Tan, Y. Wu, W. Tang, S. Song, J. Yao, Z. Wen, L. Lu, S. V. Savilov, N. Hu, J. Molenda, *Nanomaterials* **2020**, *10*.
- [95] C. Tao, M.-H. Gao, B.-H. Yin, B. Li, Y.-P. Huang, G. Xu, J.-J. Bao, *Electrochim. Acta* **2017**, *257*, 31–39.
- [96] Z. Wan, D. Lei, W. Yang, C. Liu, K. Shi, X. Hao, L. Shen, W. Lv, B. Li, Q.-H. Yang, F. Kang, Y.-B. He, *Adv. Funct. Mater.* **2019**, *29*, 1805301.
- [97] Z. Wei, Y. Ren, M. Wang, J. He, W. Huo, H. Tang, *Nanoscale Nanoscale Res. Lett.* **2020**, *15*, 122.
- [98] G. Yang, C. Chanthad, H. Oh, I. A. Ayhan, Q. Wang, *J. Mater. Chem. A* **2017**, *5*, 18012–18019.

Manuscript received: October 17, 2023

Revised manuscript received: January 11, 2024

Accepted manuscript online: January 12, 2024

Version of record online: February 2, 2024